

Research Paper

A novel route combined precursor-hydrothermal pretreatment with microwave heating for preparing holey g-C₃N₄ nanosheets with high crystalline quality and extended visible light absorption



Qiong Liu, Xueli Wang, Qian Yang, Zhengguo Zhang, Xiaoming Fang*

Key Laboratory of Enhanced Heat Transfer and Energy Conservation, The Ministry of Education, School of Chemistry and Chemical Engineering, South China University of Technology, Guangzhou, 510640, China

ARTICLE INFO

Keywords:

Photocatalysis

Holey g-C₃N₄ nanosheets

Hydrothermal pretreatment

Microwave synthesis

Hydrogen revolution

ABSTRACT

The photocatalytic water splitting for hydrogen fuel by utilizing solar energy is considered a useful route to settle the energy crisis, but a bottleneck is occurred in developing a highly efficient photocatalysts. Herein, a facile method is applied to fabricate the holey carbon nitride (HCN) nanosheets with high crystallization network and extended optical absorption region by using the hydrothermal and microwave processes. The hydrothermal treatment of dicyandiamide will enable it to transform into the melamine-cyanurate complex which would then form the ultrathin CN nanosheets with the abundant porous structure. And then the microwave-assisted thermolysis process helps the generation of g-C₃N₄ which retains the highly crystalline and the enhanced optical absorption region. Eventually, the highly crystalline network comes with the narrowed band gap and the higher specific surface area encounter in optimized g-C₃N₄ leading it exhibits a relatively high photocatalytic performance than pristine bulk carbon nitride which the hydrogen evolution rate of it reaching 81.6 μmol/h.

1. Introduction

Photodriven water splitting using semiconductor photocatalysts with visible light activity to convert solar radiation into storage and transportable energy is considered to be an efficient alternative for the confined fossil fuels [1,2]. An ideal photocatalyst should possess a broad optical absorption region, suitable energy band positions, high charge transfer efficiency and good stability [3,4]. Accordingly, numerous semiconducting materials have been explored for developing high-performance photocatalysts [5–7]. Among them, graphitic carbon nitride (CN), a metal-free polymer semiconductor, serves as a promising target material for chemical fuel conversion (e.g., H₂) [8,9], because it has the visible light response band gap (2.7 eV), relatively high reduction band position for hydrogen generation, and chemical stability. But in most cases, the application of bulk CN in photocatalysis is far away from satisfaction for photocatalytic performance due to its small specific surface area, limited active sites and low photo-induced carrier transport rate [10]. Consequently, a lot of efforts have been made on CN for increasing its photocatalytic activity.

In order to overcome the shortcomings of CN, several strategies have been explored, which include energy band engineering, coupling with other semiconductor or metals, copolymerization with organic

molecules, and designing various nanostructure [11]. Among them, preparing porous 2D CN nanosheets has been found to be one of the most efficient ways for elevating photocatalytic activity of CN, since this kind of nanostructure, compared to bulk CN, possesses larger specific surface area, promoted charge carriers transport ability and enhanced active sites, owing to its structural features [12–14]. As a result, the enhanced photocatalytic efficiency has been achieved by those porous 2D CN nanosheets. Generally, a top-down process is employed for preparing 2D CN nanosheets, which involves exfoliating bulk CN via sonication in various polarity solvents [15,16], conducting protonated modification with liquid acids, such as H₂SO₄, HCl, HNO₃ and H₃PO₄ [17–19], or thermally etching bulk CN under H₂, NH₃ or Ar atmosphere [20–22]. However, it is notable that these top-down preparation procedures usually suffer from some essential drawbacks, such as low yield, time consuming and hazardous gas generation. Apparently, novel facile routes for preparing porous 2D CN nanosheets need to be explored. Recently, Qu et al. [23] prepared a “seaweed” CN architecture by hydrothermally treating dicyandiamide and freezing drying the obtained hydrothermal product using liquid nitrogen, followed by the common pyrolysis; they found that the architecture exhibited high hydrogen evolution rate. But they just put emphasis on the freezing drying and did not elucidate how the hydrothermal pretreatment affect

* Corresponding author.

E-mail address: cexmfang@scut.edu.cn (X. Fang).

the formation of the architecture. In this year, several researches concerning the hydrothermal pretreatment of melamine have been reported. Specifically, the 3D porous N-doped CN was prepared by hydrothermally treating the aqueous solution containing melamine and urea followed by the pyrolysis [24]; the CN nanosheets were obtained from the thermal polymerization of the hydrothermally treated melamine [25], and the porous CN nanosheets were prepared by hydrothermally treating the aqueous solution containing melamine and thiourea, followed by the calcination [26]. The above researches suggest that the precursor hydrothermal pretreatment seems a facile bottom-up strategy for constructing porous CN or nanosheets, but the related formation mechanism is still unclear. Therefore, more investigations need to be conducted on this strategy for reaching a rational modulation on the microstructure, optical properties and photocatalytic activity of the obtained CN nanostructures.

Furthermore, different from the common thermal polymerization, the microwave-assisted heating synthesis has been found to a rapid synthetic route for preparing CN [27]. This process involves employing microwave-absorbing materials such as CuO to absorb microwaves strongly for inducing a rapid temperature rise within several minutes, leading to greatly shortened preparation time; more importantly, the CN materials prepared by the microwave-assisted heating synthesis have been revealed to exhibit improved crystalline quality, thus favoring charge transport; as a result, the enhanced photocatalytic activity has been achieved [27–29]. One can expect that, if the microwave-assisted heating is employed to replace the thermal polymerization for preparing porous 2D CN nanosheets, the obtained nanostructures will exhibit large specific surface, abundant active sites, and enhanced crystallinity, thereby benefiting the further improvement in photocatalytic activity.

Herein, in order to obtain the high-performance CN photocatalyst with large specific surface, abundant active sites along with enhanced crystallinity, the precursor hydrothermal pretreatment was combined with the microwave-assisted heating to prepare porous CN nanosheets. Specifically, the dicyandiamide (DCDA) was first treated by the hydrothermal process to form the melamine-cyanaurate complex (MCA). Then the obtained MCA endured the microwave-assisted thermolysis to generate porous CN nanosheets. The morphology, microstructure, optical properties and photocatalytic activity of the obtained samples were investigated and compared with those of the samples obtained from DCDA directly or prepared by the conventional thermal polymerization process. It is found that the porous CN nanosheets obtained from the two-step method possess the extended visible light absorption region and increased crystalline property, which could yield the utilization of visible light and improve the separation of photo-induced carriers. As expected, the eventually synthesized sample presents highly improved photocatalytic hydrogen evolution than bulk CN under visible light. This strategy offers a promising route towards the efficient CN photocatalysts.

2. Experimental section

2.1. Sample preparation

The holey carbon nitride nanosheets were prepared by as follows: firstly, 3 g DCDA was added into a Teflon-lined stainless steel autoclave containing 15 ml water and then heated to 433 K and kept for 8 h. After the reaction completed, the product was washed and dried to obtain an intermediate. Then, the obtained intermediate was transferred to an ceramic crucible (25 ml) covered with a bigger ceramic crucible (50 ml), followed by being placed inside a 200 ml crucible that was buried with the CuO powder for absorbing the microwave. The schematic diagram of the reactor by microwave process is shown in Fig. S1. Finally, this vessel was transferred in a microwave oven (G80F20CN2LB8 (RO), 800 W power, Galanz) and treated for 25 min. The obtained sample was named as HCN-25 min. Another samples obtained under

different microwave treatment times were named as HCN-15 min, HCN-20 min, and HCN-30 min, respectively. Additionally, the intermediate was heated to 823 K at a heating rate of 5 K/min and kept for 4 h using a muffle furnace, and the obtained sample was named as HCN-823 K.

For comparison purposes, 4 g dicyandiamide (DCDA) was treated by the above microwave treatment process for 25 min, and the obtained sample was named as BCN-25 min. Another sample was obtained from the thermal polymerization of DCDA at 823 K for 4 h, which was named as BCN-823 K.

2.2. Characterization

X-ray diffraction (XRD) patterns were recorded by a Rigaku D/max-2200 V diffractometer, using Cu K α 1 radiation. The infrared absorption spectra (FT-IR) were analyzed by a Bruker Vector 33 Fourier transform infrared spectrophotometer. The morphologies of the samples were observed by a Hitachi SU8220 scanning electron microscope (SEM), a JEOL JEM-2100 F transmission electron microscopes (TEM). UV-vis diffuse reflectance spectra (DRS) was investigated on a Shimadzu UV-3600 UV-vis spectrophotometer. The surface composition and the chemical environment was obtained by using a Kratos Axis Ultra DLD X-ray photoelectron spectroscopy (XPS). Elemental analysis of carbon and nitride were used an Elementar Varia EL cube.

Photoluminescence (PL) emission spectra was recorded with a Hitachi F-4600 spectrometer with a 375 nm of excitation wavelength. Nitrogen adsorption–desorption isotherms were acquired at 77 K by a Micromeritics ASAP 2020 apparatus. Solid electron spin resonance (ESR) signals were measured by a Bruker model A300 spectrometer at room temperature. Thermogravimetric analysis (TGA) was monitored via a Netzsch STA449 F3 at a heating rate of 5 K/min from 308 K to 1073 K with inflating N₂. Electrochemical properties were carried out by a CHI660E electrochemical workstation (Chenhua, Shanghai) via a conventional three-electrode system with Pt wire and an Ag/AgCl electrode as counter electrode and reference electrode, respectively. Working electrodes were fabricated by dip-coating the as-prepared catalyst slurry onto the FTO glass electrode (1.0 × 2.0 cm²), followed by annealing at 423 K for 2 h, the working area was calibrated as 1.0 × 1.0 cm² and 0.5 M Na₂SO₄ as the electrolyte solutions.

2.3. Evaluation of photocatalytic activity

The photocatalytic hydrogen rate was investigated with an outer top-irradiation photoreactor vessel with the sealed gas circulation system. Briefly, 50 mg of the samples were dispersed into 100 ml of 10 vol% triethanolamine aqueous solution which of containing H₂PtCl₆ (Pt, 0.2% wt) used as a cocatalyst. A 300 W Xe-lamp (ProfectLight, Microsolar300) equipped with a 420 nm cutoff filter was selected as the visible light source. Before irradiation, the suspension and the gas circulation system was thoroughly degassed to assure the air release, and the reaction vessel was kept at 278 K by flowing cooling water during the whole reaction time. The evolved hydrogen was collected every hour and analyzed with an online gas chromatograph (GC7600, Tian Mei) equipped with a thermal conductive detector and nitrogen as the carrier gas.

The apparent quantum efficiency (AQE) for hydrogen revolution was measured using the same experiment setup, except for the different wavelength band-pass filters. And the AQE was calculated as (N/I), where N and I represent the atomic number of revolved H₂ and the number of incident photons. The intensity of incident photons are measured by irradiatometer Newport 91150.

3. Results and discussion

3.1. Structure and morphology

The morphologies of the obtained samples have been investigated

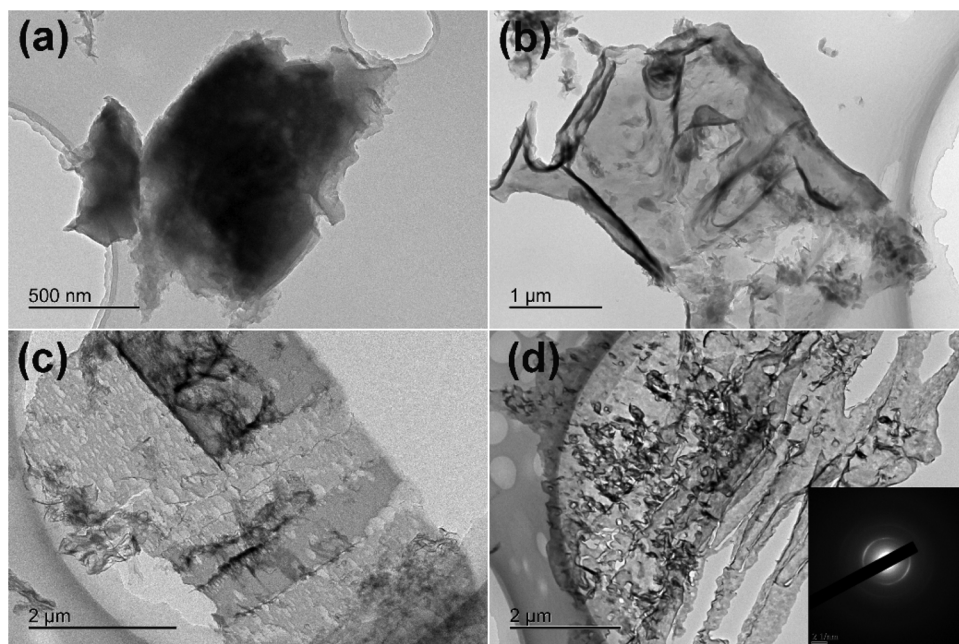


Fig 1. TEM images of BCN-823 K (a), BCN-25 min (b), HCN-823 K (c) and HCN-25 min (d), respectively.

by TEM and SEM, as shown in Figs. 1 and S2 (Supporting Information). Both BCN-823 K and BCN-25 min show the large irregular particles, but the surface of BCN-25 min is smoother than the former. When the precursor DCDA has experienced the hydrothermal treatment, the gained HCN-823 K and HCN-25 min samples both exhibit obvious thin but crinkled nanosheets, which own the abundant in-plane macro/mesoporous network (Fig. S2c, d). The TEM image in Fig. 1c also clearly reveals the HCN-823 K renders the large scale two-dimension lamellar structure, which contains the nanosized pores with diameters ranging from 20 nm to about 300 nm. It means after the DCDA endured the hydrothermal treatment, the holey thin CN nanosheets have been synthesized. When compared to HCN-823 K, HCN-25 min obtained from the microwave heating process has the similar porous nanosheets framework, and some of the edge of in-plane pores show relatively the deeper contrast, suggesting its more thickness or the high crystalline layers. From the inset SAED image of Fig. 1d, a bright diffraction ring could be obviously found, which lattice distance could roughly be measured to be 0.322 nm, indexed to the characteristic (002) crystal face of CN [30]. This result demonstrates HCN-25 min possesses the high crystallinity along with the porous nanosheets structure. In order to learn the specific surface area and pore structure, the N_2 sorption–desorption isotherms of the obtained samples are collected in Fig. 2a, the BET surface area of HCN-823 K is measured to be $95.04\text{ m}^2/\text{g}$, which is much higher than those of BCN-823 K ($8.22\text{ m}^2/\text{g}$) and BCN-25 min ($6.84\text{ m}^2/\text{g}$). And HCN-25 min ($31.64\text{ m}^2/\text{g}$) has the smaller surface area than HCN-823 K, due to the promoted crystallinity, but it is still about 3.85 and 4.62 folds those of BCN-823 K and BCN-25 min. Correspondingly, the pore volume of HCN-823 K ($0.457\text{ cm}^3/\text{g}$) and HCN-25 min ($0.172\text{ cm}^3/\text{g}$) are obviously larger than BCN-823 K ($0.048\text{ cm}^3/\text{g}$) and BCN-25 min ($0.038\text{ cm}^3/\text{g}$). The increased surface area and pore volume are resulted from the crinkled thin nanosheets and the presence of the in-plane pores [12]. Further insight into the pore size distribution plots (the inset of Fig. 2a), both HCN-823 K and HCN-25 min show a broad distribution over the range of 20 nm to 400 nm, implying the macro/mesoporous structure are well generated. While BCN-823 K and BCN-25 min just render the limited pore size distribution. It needs to noted that, the enhanced surface area and macro/mesoporous structure for HCN-823 K and HCN-25 min usually render them with more active sites and higher mass transform efficiency, both of which are favorable for the photocatalytic activity [20]. Additionally, seen from Fig. S3 and Table S1, the specific surface area of

the other samples under the different microwave time mostly exhibit the similar value.

The XRD patterns and FTIR spectra have been measured to learn the physical structure information. The XRD pattern (Fig. S4) of the intermediate, obtained from the hydrothermal treatment of DCDA, exhibits a big difference from that of DCDA, which could be indexed to the melamine cyanaurate complex (MCA, JCPDS#05-0127) [31]. And the FTIR and TGA patterns (Figs. S5–S6) also present the change of the physical and thermal properties. It is suggested that the hydrothermal process could lead to the transformation from DCDA into the supramolecular intermediate. Note that, to the best of our knowledge, this is the first time demonstrated the dicyandiamide could be transformed into MCA via hydrothermal process. As this intermediate retains the in-plane 2D hexagonal pattern and also serves as the porogen, the resulted thermal polymerization CN sample HCN-823 K possesses the porous thin nanosheets structure. From Fig. 2b, all the obtained samples own two similar distinct diffraction peaks of (100) and (002), implying the basic crystal structure of CN is mostly maintained after modification [32]. Compared to BCN-823 K, the two diffraction peaks of HCN-823 K became less pronounced, originated from the reduced lamellar size. And an obvious shift of the (002) peak from 27.34° to 27.54° is observed, demonstrating the interlayer distance of the graphitic like planar is reduced from 0.352 nm to 0.327 nm , which is contributed to the thinner nanosheets [33,34]. The samples (BCN-25 min and HCN-25 min) via the microwave process could exhibit the relatively higher intensity of diffraction peaks, and a new (110) peak at 21.6° is investigated, which indicate the enhanced crystallinity, in accord with the aforementioned TEM results [28]. Henceforth, this could lead to the denser packing of the layers in HCN-25 min than that in HCN-823 K, and thus the correspondingly shift of (002) peak from 27.54° to 27.76° is occurred (Fig. 2c). For the other hand, as the microwave time extended, the intensity of the diffraction peaks is increased (Fig. S7), indicating the microwave treatment has the effect on the crystalline property. Fig. 2d shows the FTIR spectra of BCN-823 K, BCN-25 min, HCN-823 K and HCN-25 min, both of them show the typical CN molecular band. In details, the broad band between $3000\text{--}3600\text{ cm}^{-1}$ is assigned to the $-\text{NH}_2$ or the absorbed H_2O molecular. The set of strong peaks among $1200\text{--}1800\text{ cm}^{-1}$ are ascribed to skeletal vibration of C–N heterocycles, and an intense peak at 808 cm^{-1} is indexed to the characteristic triazine cycles [26].

The compositions and chemical states of HCN-25 min was analyzed

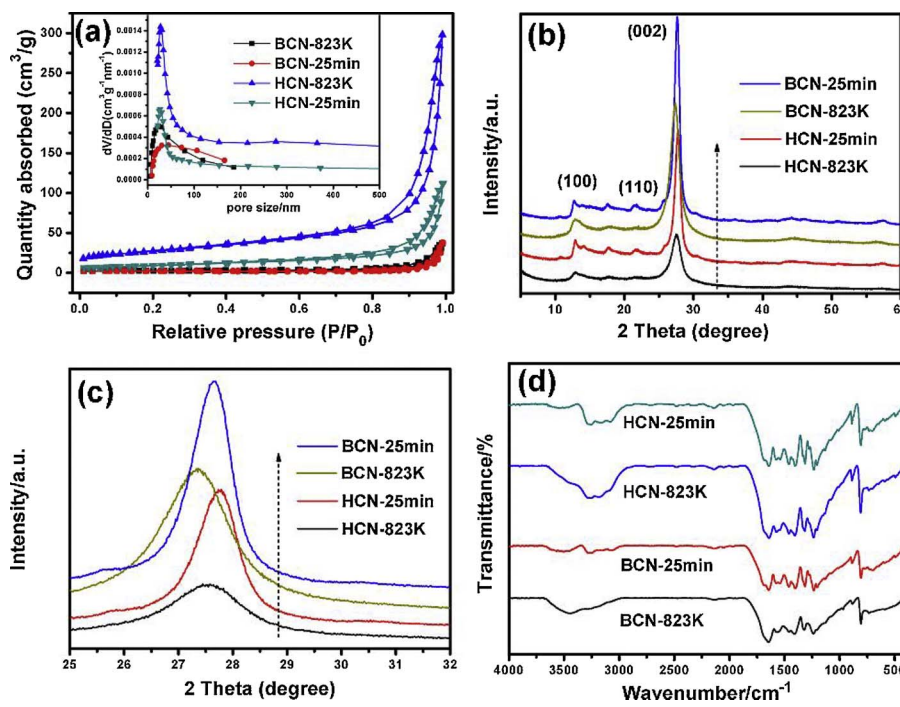


Fig. 2. (a) N₂ adsorption-desorption isotherms, (b) XRD patterns, (c) the (002) peak of XRD patterns and (d) FTIR spectra of BCN-823 K, BCN-25 min, HCN-823 K and HCN-25 min. The inset image in Fig. 2a is the pore size distribution plots.

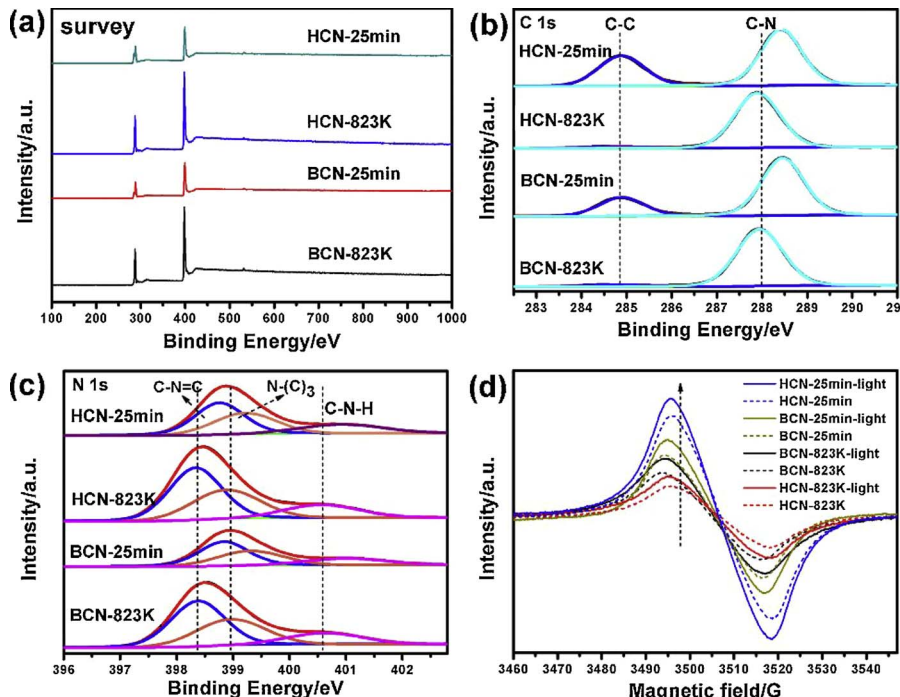


Fig. 3. XPS spectra of survey (a), the high resolution C 1s spectra (b), the high resolution N 1s (c) and room-temperature solid-state EPR spectra (d) of electron in the dark or measured with visible light ($\lambda > 420$ nm) under atmospheric conditions for BCN-823 K, BCN-25 min, HCN-823 K and HCN-25 min.

Table 1
Physicochemical properties of BCN-823 K, BCN-25 min, HCN-823 K and HCN-25 min.

Samples	S_{BET} (m ² g ⁻¹)	PV ^a (cm ³ g ⁻¹)	$N_{\text{2C}}/N_{\text{3C}}$ ^b	N/C from XPS	N/C molar ratio	E_g^c (eV)
BCN-823 K	8.22	0.048	1.447	1.402	1.456	2.68
BCN-25 min	6.84	0.038	1.383	1.080	1.442	2.53
HCN-823 K	95.04	0.457	1.485	1.357	1.446	2.77
HCN-25 min	31.64	0.172	1.306	0.925	1.439	2.46

^a PV: Pore Volume.

^b $N_{\text{2C}}/N_{\text{3C}}$: (XPS, $N_{\text{2C}}:C-N=C$, $N_{\text{3C}}:N-(C)_3$).

^c E_g : energy gap.

by XPS technology. From the high resolution C 1s spectra in Fig. S8, two C 1s peaks located at 284.8 eV and 288.4 eV are indexed to C–C and N=C–N, respectively [21]. The N 1s spectrum (Fig. S9) could be deconvoluted into three peaks at 398.8, 399.2, 400.9 eV which are derived from C=N–C, N–(C)₃ and C–N–H, respectively [12]. When compared the mentioned samples, the same three elements including C, N and O are observed in the survey spectrum in Fig. 3a. And as the addition of CuO power to absorb the microwave under the polymerization process, so the Cu 2p of HCN-25 min is also conducted in Fig. S10 to verify the absence of Cu element in the sample. And no signal peaks are observed, implying there aren't Cu species involved in the gained sample. The comparison of BCN-823 K, BCN-25 min, HCN-

823 K and HCN-25 min over the C 1s and N 1s spectrums are shown in Fig. 3b and c. The same peak position of C–C binding is investigated for the related samples, but the obviously enhanced binding energy of N=C–N peaks are appeared in BCN-25 min and HCN-25 min, compared to BCN-823 and HCN-823 K. Correspondingly, the N=C–N peaks and N–(C)₃ over the N 1s spectrums also possess the right shift of binding energy. These may due to charge effect originated from the presence of nitrogen vacancies and the N long-pair electrons occupied π orbitals of C–N bonds [35]. As expected, the calculated peak area ratios (from XPS N 1s data) of N₂C to N₃C decrease from 1.485 in HCN-823 K to 1.306 in HCN-25 min and 1.447 in HCN-823 K to 1.383 in BCN-25 min (Table 1). In addition, the N/C molar ratios via elementary analysis (EA) are 1.439 for HCN-25 min and 1.442 for BCN-25 min, which are lower than BCN-823 K (1.456) or HCN-823 (1.446), as listed in Table 1. Therefore, the CN samples (BCN-25 min and HCN-25 min) endured the microwave process might lead to the generation of nitrogen vacancies [36]. When combined with the surface atomic ratio of N/C measured via XPS which exhibits the pronounced N species loss than bulk elementary analysis, it is inferred that the nitrogen vacancies prone to generating around the surface or the edge of the obtained composites [30]. The surface nitrogen vacancies usually facilitate the charge separation, increase the mobility of photo-induced charge carriers and also have good influence on the optical absorption property [37]. Fig. 3d shows the solid electron paramagnetic resonance (EPR) spectrums for the prepared samples to examine the electronic band structure and charge transfer properties. The central symmetry EPR peaks at 3505 G ($g = 2.03$) are investigated for the related samples, which are assigned to the delocalized unpaired electrons of the aromatic π -conjugated rings. Both BCN-25 min and HCN-25 min show the increased EPR intensity than BCN-823 K, revealing the better established electron band structure and HCN-25 min possesses the larger intensity than other samples, indicating its optimized π -conjugated system which leads to greater chance for separating charge carriers and the higher mobility of charge transfer [38]. While the HCN-823 K has the lowest intensity of EPR signal, this may due to the low crystalline or the relatively imperfection C–N heterocycles. Therefore, in this case, as the synergistic effects of the porous nanosheets and the high crystalline property over HCN-25 min which could lead to the highest EPR intensity. Under visible light irradiation, all the samples show the enhanced intensity of EPR peaks, demonstrating the sensitive visible light response for photocatalytic application. And as expected, HCN-25 min also owns the highest value of EPR signal, indicating the better transfer mobility of photo-induced carrier pairs [39]. Therefore, when compared to the high temperature calcination process, the synthesized CN samples via microwave polymerization could gain the more optimized aromatic π -conjugated system. What's more, as shown in Fig. S11, the intensity of EPR peak is gradually promoted as the extended time of microwave treatment and HCN-25 min presents the highest value. When the microwave time is 30 min, the EPR intensity could be decayed which might due to the destruction of the layered structure as the excess polymerization time.

3.2. Band structure and photophysical behaviour of charge carriers

The optical properties are evaluated through UV-vis diffuse reflectance (DRS) spectra, as shown in Fig. 4a, Compared to BCN-823 K, HCN-823 K presents a blue shift of the intrinsic absorption edge, assigning to the quantum confinement resulted from the thin nanosheets with holey microstructure [40]. For both BCN-25 min and HCN-25 min, an additional absorption peak ranged from 430 nm to 600 nm is appeared which is contributed to the appearance of nitrogen vacancies or the intrinsic electronic transition via $\pi \rightarrow \pi^*$ and $n \rightarrow \pi^*$ transitions [41,42]. Moreover, compared to BCN-25 min, HCN-25 min possesses a slightly enhanced region over the visible light region, due to the holey microstructure could resulted in the multiple light scattering effects. Further analysis is conducted about the calculated band gap in the inset

of Fig. 4a and Table 1, HCN-823 K shows the enlarged band gap of 2.77 eV. BCN-25 min and HCN-25 min are 2.53 eV and 2.46 eV, relatively, which are obvious small than BCN-823 K (2.68 eV). Additionally, Fig. S12 shows the DRS spectrum of the different microwave time samples, HCN-25 min and HCN-30 min show an apparent absorption shoulder ranged from 450 nm to 600 nm, while this can't be found over the shorter microwave treatment samples. This result demonstrates the microwave time plays an important role in extending the visible absorption region. To investigate the charge carriers recombination behaviour, the photoluminescence (PL) spectra are conducted in Fig. 4b, HCN-823 K exhibits slightly retarded intensity of PL emission peak than BCN-823 K of which indicating its porous nanosheets could relatively reduce the recombination of photo-induced charge carriers to some extent [25]. However, it is observed that HCN-25 min exhibits the much constrained PL peak. When compared to HCN-823 K, it means the carriers recombination behaviour of HCN-25 min is obviously suppressed, demonstrating the higher crystalline would lead to the faster separation of charge carriers [43]. And HCN-25 min also possesses the reduced intensity of PL peak than BCN-25 min, as the presence of the porous network over the nanosheets. When refers to the different microwave samples of PL spectrums in Fig. S13, as the time extended, it is observed the charge pairs' recombination behaviour is effectively retarded. The photoelectrochemical properties of the selected samples were conducted by measuring the linear sweep volyammetry (LSV), transient response photocurrent and electrochemical impedance responses (EIS). As vividly shown in Fig. 4c and d, as expected, HCN-823 K and BCN-25 min show a larger value of photocurrent than BCN-823 K, but BCN-25 min is obvious smaller than HCN-823 K which might be ascribed to porous nanosheets structure would yield the visible light absorption efficiency leading to generating more electron charge. And HCN-25 min exhibits the highest photocurrent than the other samples, suggesting the higher photo-generated charge ability of which presents the great potential in the field of photocatalytic water splitting [44]. In addition, all the samples mostly display the good and reproducible response photocurrent under the repeatedly switched ON/OFF illumination cycles, indicating the reliable photoelectrochemical stability. In Fig. 4e, the smaller diameter of semicircular Nyquist plots over HCN-25 min is investigated and under visible light irradiation, the further reduced diameter is presented, implying the good photocatalytic response and retaining the decreased electron transfer resistance from the electrode to electrolyte molecule [33]. Hence, it is demonstrated HCN-25 min owns the relatively stronger ability to transform the electron to the absorbed surface reactants and also the separation efficiency of the electron-hole pairs, because of the macro/mesoporous nanosheets structure and the higher crystalline property.

3.3. Photocatalytic activity

The photocatalytic activity of the obtained samples were evaluated by measuring the photocatalytic hydrogen evolution, which was conducted from 10% triethanolamine aqueous under visible light illumination ($\lambda > 420$ nm) and 0.2% wt H₂PtCl₆ served as cocatalyst. As displayed in Fig. 5a, the average hydrogen evolution rate (HER) of HCN-823 K is 55.3 $\mu\text{mol}/\text{h}$, which is apparently larger than BCN-823 K (7.15 $\mu\text{mol}/\text{h}$) which attributed to the enhanced specific surface area and the thin two-dimension layers. BCN-25 min also possesses the higher HER value (12.35 $\mu\text{mol}/\text{h}$) than BCN-823 K, This is due to increased visible absorption region and retarded charge carriers recombination. And the highest HER value is occurred in HCN-25 min of which reaches 81.58 $\mu\text{mol}/\text{h}$, is 1.48, 6.61 and 11.41 folds of HCN-823 K, BCN-25 min and BCN-823 K, respectively. It is implied the combined holey nanosheets, increased optical absorption and enhanced crystalline could have a profound effect for facilitating the HER results. To confirm the primary driving force of the photocatalytic performance, the comparison of the DRS spectra and wavelength dependence of

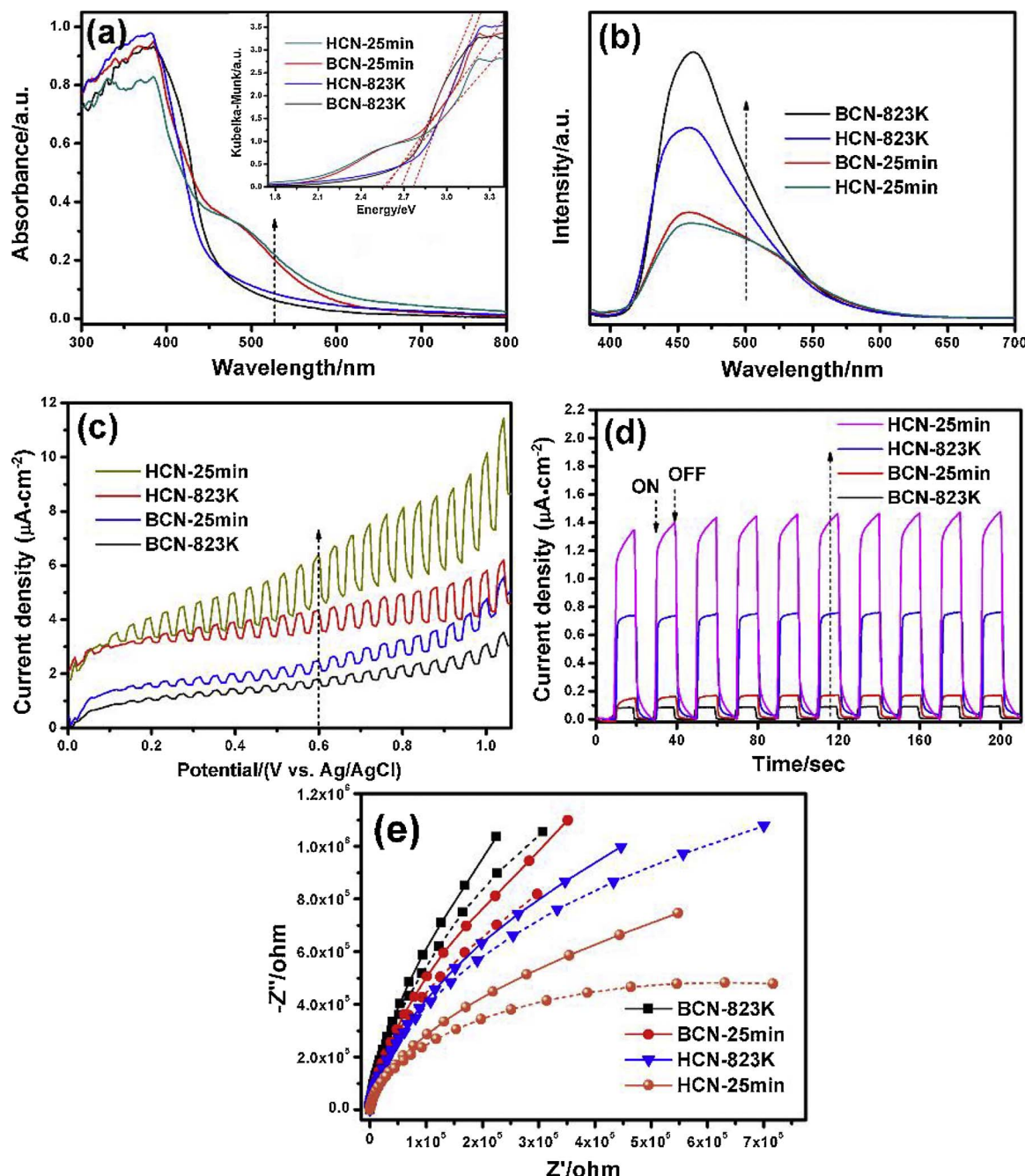


Fig. 4. (a) UV-vis diffuse reflectance spectra (DRS), (b) photoluminescence (PL) emission spectra, (c) average chopped linear sweep voltammetry (LSV) scans plots, (d) Periodic ON/OFF photocurrent response in 0.5 M Na_2SO_4 electrolyte under visible light irradiation ($\lambda > 420$ nm) at 0.5 V vs. Ag/AgCl electrode and (e) electrochemical impedance spectroscopy Nyquist plots in the dark and visible light illumination (dotted line) of BCN-823 K, BCN-25 min, HCN-823 K and HCN-25 min.

apparent quantum efficiency (AQE) over HCN-25 min are obtained in Fig. 5b. It is found that the AQE value is well coincidence with the optical absorption region and as with the wavelength prolonged, the AQE value is gradually reduced, suggesting the absorption of optical photons is the main primary force in the photocatalytic performance. The AQE value over different wavelength $\lambda = 380 \pm 15$ nm, 420 ± 15 nm, 465 ± 15 nm is 4.6%, 2.1%, 1.6%, respectively, demonstrating the relatively good optical absorption utilization. What's more, a small AQE value is investigated at $\lambda = 510 \pm 15$ nm, indicating HCN-25 min has the sensitive photocatalytic activity along with the increased visible light absorption. But it need to note that no signal of hydrogen revolution peaks are observed over the $\lambda = 565 \pm 15$ nm and $\lambda = 600 \pm 15$ nm, these might due the detection limit as the low HER. Therefore, further analysis via the

photocurrent response plots along the different wavelength by using band-pass filters is carried out in Fig. 5c, the variation trend of the photocurrent value is almost in accord with the AQE results as the wavelength changes. However, somewhat differently, it is found that both over the $\lambda = 565 \pm 15$ nm and $\lambda = 600 \pm 15$ nm, HCN-25 min electrode exhibits the relatively small photocurrent along with the several ON/OFF illumination cycles. It is demonstrated as the optical absorption region increased to 650 nm, the responsive wavelength range of HCN-25 min for the photocatalytic hydrogen revolution is extended to about 600 nm. The photocurrent response of the FTO substrate is illustrated in Fig. S14, under the visible light illumination, it can't be observed the clearly photo-driven current response which could exclude the impact of the substrate. Additionally, the HER of the different microwave time samples are also conducted in Fig. 5d, HCN-

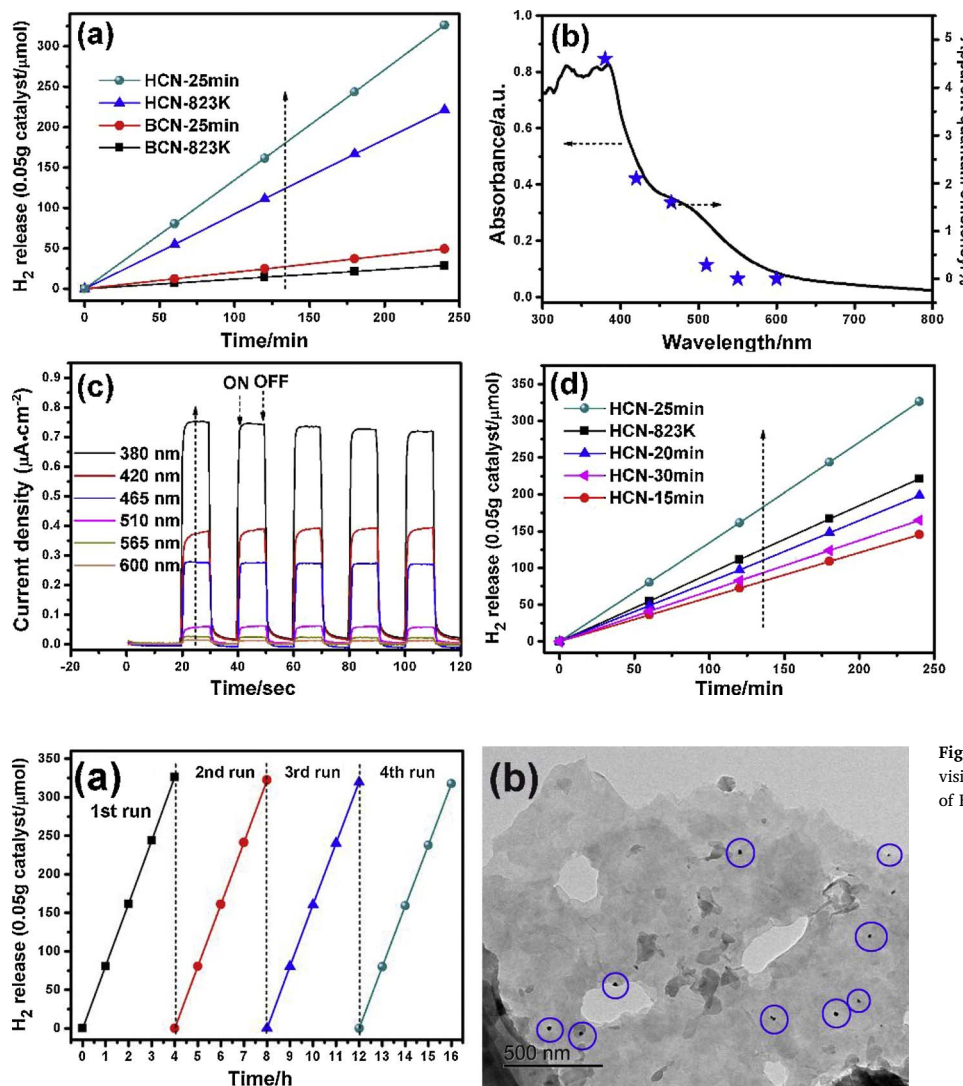


Fig. 5. (a) photocatalytic hydrogen evolution plots of BCN-823 K, BCN-25 min, HCN-823 K and HCN-25 min, (b) wavelength dependent apparent quantum efficiency over HCN-25 min with the different band-pass filters, (c) wavelength dependent photocurrent response plots over HCN-25 min with the ON/OFF illumination cycles and (d) photocatalytic hydrogen evolution plots of HCN-823 K, HCN-15 min, HCN-20 min, HCN-25 min and HCN-30 min.

15 min owns a relatively lower HER value (36.25 μmol/h) which attributed to the smaller optical absorption region and the higher recombination probability of photo-induced charge carriers. And as the microwave extended, the HER could be enhanced and HCN-25 min shows the higher value, so the optimized microwave time is selected at 25 min. When the microwave time continuously extended to 30 min, the HER of HCN-30 min is decreased. When combined the related results of XRD, DRS and PL, these could be found that the higher crystalline, increased visible absorption and retarded charge carriers recombination are occurred over HCN-30 min, but from the EPR and EA results, as the excess microwave treatment time might lead to higher degree of graphitization on CN which could be adverse to the photo-induced hydrogen generation [21]. For another, to verify the stability of the prepared photocatalyst, the time course of H₂ evolution over HCN-25 min is carried out (Fig. 6a). Under 4 h continuous irradiation, the yield of H₂ evolution almost enhances linearly. And the HER value does not present obvious deactivation after four cycles experiment, suggesting the well photocatalytic stability of HCN-25 min. What's more, from the TEM images of HCN-25 min after reaction in Fig. 6b, it's clearly found many nanoparticles are well distributed on the surface of HCN-25 min of which still retaining the macro/mesoporous nanosheets structure. It is means the successful reduction from Pt⁴⁺ to noble metal Pt via the in-situ photodeposition method and HCN-25 min could keep the similar porous but high crystalline nanosheets structure after reaction. And the XRD and FTIR spectrums of the fresh and used HCN-

25 min are displayed in Fig. S15, after the photocatalytic reaction, the HCN-25 min mostly maintains unchanged, implying robust stability of the physical structure. Therefore, based on the aforementioned results, the enhancement of the photocatalytic activity of HCN-25 min can be referred to the following reasons. First, the enhanced BET surface area with the micro/mesoporous structure via the hydrothermal treatment with DCDA enables HCN-25 min with more absorbed active catalytic sites and channels to facilitate the photocatalytic reaction. Second, the reduced band gap, the increased optical absorption region and the existence of nitrogen vacancies under the microwave process could counteract the blue shift of absorption band edge over the porous thin nanosheets and maximize photon harvest capability. Third, HCN-25 min owns the optimized π-conjugated system and higher crystalline structure, leading to the improved separation efficiency of charge carriers and significantly retarded recombination of photo-induced electron-hole pairs, which is responsible for its enhancement in photocatalytic hydrogen evolution. At last, it need to note the photocatalytic activity is controlled by a compromise between the several factors, such as the wide optical absorption, the specific surface area and the crystalline of the structure. Therefore, the optimized and suitable factors are critical to be found to gain the higher photocatalytic activity.

4. Conclusions

In summary, we developed a novel HCN-25 min sample which owns

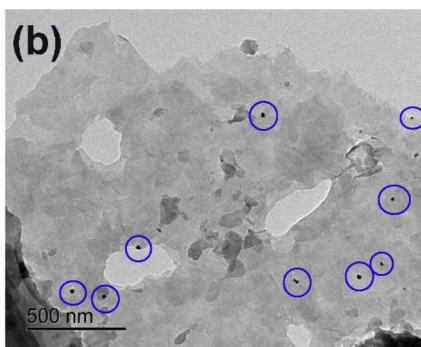


Fig. 6. (a) time course of H₂ release for HCN-25 min under visible light irradiation ($\lambda > 420$ nm) and (b) TEM images of HCN-25 min after the reaction.

the hole nanosheets structure, reduced band gap and also with the high crystalline through a simple hydrothermal treatment and then microwave process. The hydrothermal treatment of DCDA leads to formation the MCA aggregates which further result in the generation of thin nanosheets with micro/mesoporous structure, this could enhance the surface absorbed active sites and yield the optical absorption utilization factor. And the microwave polymerization process enables HCN-25 min to possess the enhanced visible absorption region, the reduced band gap, the highly crystalline and retarded recombination of charge carriers. As these related synergic advantages, HCN-25 min exhibits good photocatalytic activity which the HER value reaches to 81.58 $\mu\text{mol}/\text{h}$. This work provides a new button-up strategy for fabrication of holey CN nanosheets with the large enhanced visible light absorption and highly crystalline for optimized photocatalytic activity. And this results pave the way for exploration the materials which both retain the narrowed band gap and reduced thickness layer.

Acknowledgements

This work was financially supported by the National Natural Science Foundation of China (21276088 and U1507201) and Natural Science Foundation of Guangdong Province (2014A030312009).

Appendix A. Supplementary data

Supplementary data associated with this article can be found, in the online version, at <http://dx.doi.org/10.1016/j.apcatb.2017.11.044>.

References

- [1] S.U.M. Khan, M. Al-Shahry, W.B. Ingler, *Science* 297 (2002) 2243–2245.
- [2] A. Kudo, Y. Miseki, *Chem. Soc. Rev.* 38 (2009) 253–278.
- [3] K. Maeda, K. Domen, *J. Phys. Chem. Lett.* 1 (2010) 2655–2661.
- [4] J. Schneider, M. Matsuoka, M. Takeuchi, J. Zhang, Y. Horiuchi, M. Anpo, D.W. Bahnemann, *Chem. Rev.* 114 (2014) 9919–9986.
- [5] T. Hisatomi, J. Kubota, K. Domen, *Chem. Soc. Rev.* 43 (2014) 7520–7535.
- [6] X. Zou, Y. Zhang, *Chem. Soc. Rev.* 44 (2015) 5148–5180.
- [7] F.E. Osterloh, *Chem. Soc. Rev.* 42 (2013) 2294–2320.
- [8] X. Wang, K. Maeda, A. Thomas, K. Takanabe, G. Xin, J.M. Carlsson, K. Domen, M. Antonietti, *Nat. Mater.* 8 (2009) 76–80.
- [9] J. Liu, Y. Liu, N. Liu, Y. Han, X. Zhang, H. Huang, Y. Lifshitz, S.-T. Lee, J. Zhong, Z. Kang, *Science* 347 (2015) 970–974.
- [10] F.K. Kessler, Y. Zheng, D. Schwarz, C. Merschjann, W. Schnick, X. Wang, M.J. Bojdys, *Nat. Rev. Mater.* 2 (2017) 17030.
- [11] W.-J. Ong, L.-L. Tan, Y.-H. Ng, S.-T. Yong, S.-P. Chai, *Chem. Rev.* 116 (2016) 7159–7329.
- [12] Q. Liang, Z. Li, X. Yu, Z.-H. Huang, F. Kang, Q.-H. Yang, *Adv. Mater.* 27 (2015) 4634–4639.
- [13] Q. Han, B. Wang, J. Gao, Z. Cheng, Y. Zhao, Z. Zhang, L. Qu, *ACS Nano* 10 (2016) 2745–2751.
- [14] K.S. Lakhi, D.-H. Park, K. Al-Bahily, W. Cha, B. Viswanathan, J.-H. Choy, A. Vinu, *Chem. Soc. Rev.* 46 (2017) 72–101.
- [15] X. Zhang, X. Xie, H. Wang, J. Zhang, B. Pan, Y. Xie, *J. Am. Chem. Soc.* 135 (2013) 18–21.
- [16] S. Yang, Y. Gong, J. Zhang, L. Zhan, L. Ma, Z. Fang, R. Vajtai, X. Wang, P.M. Ajayan, *Adv. Mater.* 25 (2013) 2452–2456.
- [17] Z. Zhou, J. Wang, J. Yu, Y. Shen, Y. Li, A. Liu, S. Liu, Y. Zhang, *J. Am. Chem. Soc.* 137 (2015) 2179–2182.
- [18] X. Du, G. Zou, Z. Wang, X. Wang, *Nanoscale* 7 (2015) 8701–8706.
- [19] J. Liu, J. Huang, H. Zhou, M. Antonietti, *ACS Appl. Mater. Interfaces* 6 (2014) 8434–8440.
- [20] Q. Liang, Z. Li, Z.H. Huang, F. Kang, Q.H. Yang, *Adv. Funct. Mater.* 25 (2015) 6885–6892.
- [21] Y. Kang, Y. Yang, L.C. Yin, X. Kang, G. Liu, H.M. Cheng, *Adv. Mater.* 27 (2015) 4572–4577.
- [22] P. Niu, L.C. Yin, Y.Q. Yang, G. Liu, H.M. Cheng, *Adv. Mater.* 26 (2014) 8046–8052.
- [23] Q. Han, B. Wang, Y. Zhao, C. Hu, L. Qu, *Angew. Chem. Int. Ed.* 54 (2015) 11433–11437.
- [24] N. Tian, Y. Zhang, X. Li, K. Xiao, X. Du, F. Dong, G.I.N. Waterhouse, T. Zhang, H. Huang, *Nano Energy* 38 (2017) 72–81.
- [25] Y.Z. Hong, C.S. Li, Z.Y. Fang, B.F. Luo, W.D. Shi, *Carbon* 121 (2017) 463–471.
- [26] H. Huang, K. Xiao, N. Tian, F. Dong, T. Zhang, X. Du, Y. Zhang, *J. Mater. Chem. A* 5 (2017) 17452–17463.
- [27] Y.-P. Yuan, L.-S. Yin, S.-W. Cao, L.-N. Gu, G.-S. Xu, P. Du, H. Chai, Y.-S. Liao, C. Xue, *Green Chem.* 16 (2014) 4663–4668.
- [28] H. Liu, D. Chen, Z. Wang, H. Jing, R. Zhang, *Appl. Catal. B: Environ.* 203 (2017) 300–313.
- [29] Y. Guo, J. Li, Y. Yuan, L. Li, M. Zhang, C. Zhou, Z. Lin, *Angew. Chem. Int. Ed.* 55 (2016) 14693–14697.
- [30] X. Ji, X. Yuan, J. Wu, L. Yu, H. Guo, H. Wang, H. Zhang, D. Yu, Y. Zhao, *ACS Appl. Mater. Interfaces* 9 (2017) 24616–24624.
- [31] J. Xu, H. Wang, C. Zhang, X. Yang, S. Cao, J. Yu, M. Shalom, *Angew. Chem. Int. Ed.* 56 (2017) 8426–8430.
- [32] Q. Liu, Y. Guo, Z. Chen, Z. Zhang, X. Fang, *Appl. Catal. B: Environ.* 183 (2016) 231–241.
- [33] J. Ran, T.Y. Ma, G. Gao, X.-W. Du, S.Z. Qiao, *Energy Environ. Sci.* 8 (2015) 3708–3717.
- [34] Q. Liu, T. Chen, Y. Guo, Z. Zhang, X. Fang, *Appl. Catal. B-Environ.* 193 (2016) 248–258.
- [35] Q. Tay, P. Kanhere, C.F. Ng, S. Chen, S. Chakraborty, A.C.H. Huan, T.C. Sum, R. Ahuja, Z. Chen, *Chem. Mater.* 27 (2015) 4930–4933.
- [36] L.J. Fang, X.L. Wang, J.J. Zhao, Y.H. Li, Y.L. Wang, X.L. Du, Z.F. He, H.D. Zeng, H.G. Yang, *Chem. Commun.* 52 (2016) 14408–14411.
- [37] P. Niu, G. Liu, H.-M. Cheng, *J. Phys. Chem. C* 116 (2012) 11013–11018.
- [38] Q. Liu, T. Chen, Y. Guo, Z. Zhang, X. Fang, *Appl. Catal. B-Environ.* 205 (2017) 173–181.
- [39] Y. Nosaka, M. Nishikawa, A.Y. Nosaka, *Molecules* 19 (2014) 18248–18267.
- [40] Q. Han, Z. Cheng, J. Gao, Y. Zhao, Z. Zhang, L. Dai, L. Qu, *Adv. Funct. Mater.* 27 (2017) 1606352.
- [41] Y. Chen, B. Wang, S. Lin, Y. Zhang, X. Wang, *J. Phys. Chem. C* 118 (2014) 29981–29989.
- [42] G. Fanchini, A. Tagliaferro, N.M.J. Conway, C. Godet, *Phys. Rev. B* 66 (2002) 195415.
- [43] H. Ou, L. Lin, Y. Zheng, P. Yang, Y. Fang, X. Wang, *Adv. Mater.* 29 (2017) 1700008.
- [44] J. Bian, L. Xi, C. Huang, K.M. Lange, R.-Q. Zhang, M. Shalom, *Adv. Energy Mater.* 6 (2016) 1600263.